Cellulose (2022) 29:5493–5509
https://doi.org/10.1007/s10570-022-04603-9

ORIGINAL RESEARCH

Viscoelastic-mapping of cellulose nanofibrils using low-total-force contact resonance force microscopy (LTF-CRFM)

Kristen M. Hess · Jason P. Killgore · Ashutosh Mittal · Wil V. Srubar III

Received: 9 August 2021 / Accepted: 19 April 2022 / Published online: 26 May 2022

Abstract Low-total-force contact resonance force microscopy (LTF-CRFM), an atomic force microscopy method, is introduced as a non-destructive means to quantify the local viscoelastic loss tangent (tanδ) of supported cellulose nanofibrils (CNFs). The method limits static and dynamic forces during measurement to minimize substrate and geometry effects and to reduce the potential for stress-induced CNF damage. LTF-CRFM uses Brownian motion to achieve the thermally-limited lowest dynamic force, while approaching adhesive pull-off to achieve the low static force. LTF-CRFM measurements were shown to generate analyzable data without evidence of nonlinear artifacts and without damage to the CNF over static forces ranging from 11.6 to 84.6 nN. The measured tanδ of CNFs was 0.015 ± 0.0094, which is the first reported tanδ measurement of an isolated CNF. Finally, LTF-CRFM successfully mapped tanδ along the length of CNFs to determine that kink defects along the CNF do not impart a local viscoelastic property change at the spatial resolution of the measurement.

Keywords Cellulose nanofibril · Contact resonance force microscopy · Brownian motion · Viscoelastic loss tangent

Supplementary Information The online version contains supplementary material available at https://doi.org/10.1007/s10570-022-04603-9.

K. M. Hess · W. V. Srubar III
Department of Civil, Environmental, and Architectural Engineering, University of Colorado Boulder, ECOT 441 UCB 428, Boulder, CO 80309-0428, USA

J. P. Killgore (✉)
Applied Chemicals and Materials Division, National Institute of Standards and Technology, Boulder, CO 80305, USA
e-mail: jason.killgore@nist.gov

A. Mittal
Renewable Resources and Enabling Sciences Center, National Renewable Energy Laboratory, 15013 Denver West Parkway, Golden, CO 80401, USA

W. V. Srubar III
Materials Science and Engineering Program, University of Colorado Boulder, UCB 613, Boulder, CO 80303, USA

Introduction

Cellulose is a linear polymer chain comprised of glucose rings connected through glycosidic bonds (Azizi Samir et al. 2005; Moon et al. 2011; Heinze 2015). Hydrogen bonding between hydroxyl groups and oxygen molecules on neighboring glucose rings stabilize the glycosidic bonds, which leads to the linear configuration of cellulose. Hydroxyl groups and oxygen molecules from separate linear chains interact through hydrogen bonding to form parallel assemblies. The

aggregation of the parallel assemblies form cellulose fibrils that are 5–50 nm in diameter and several microns in length. The hydrogen bonding makes cellulose a relatively stable polymer and provides the cellulose fibrils with high axial elastic modulus (i.e., 110–220 GPa) (Moon et al. 2011). Cellulose has many advantageous attributes including bio-renewability, low cost, widespread availability and high-performance mechanical properties (Moon et al. 2011; Heinze 2015; Wagner et al. 2016; Aydemir and Gardner 2020). As such, cellulose has been processed into microscale or nanoscale materials, such as cellulose nanocrystals (CNCs) or cellulose nanofibrils (CNFs) (Wagner et al. 2016), for applications ranging from transparent films for electronic displays (Purandare et al. 2014) to biocompatible hydrogels for biomedical technologies (Curvello et al. 2019).

This work focuses on CNFs, which are mechanically separated into rod-like anisotropic structures with nanometer-scale diameters and micron-scale lengths (Zhang et al. 2013; Wagner et al. 2016). Moreover, previous investigation has found CNFs have heterogeneities, namely in its structure (Zhang et al. 2013) and mechanically-induced deformations (Ciesielski et al. 2019). CNFs contain alternating highly ordered crystalline regions and disordered amorphous regions (Zhang et al. 2013), where the elastic modulus is expected to be greater in the crystalline region compared to the amorphous region since the crystalline cellulose modulus is 5–10 times greater than the modulus of the CNF (Nishiyama 2009). For cellulose derived from plant species, the degree of crystallinity typically varies from 40 to 70% depending on the source species and processing technique (Mariano et al. 2014; Nechyporchuk et al. 2016). In addition, isolated CNFs have observable kinked defects, which are mechanically induced ex-situ from, for example, processing conditions (Usov et al. 2015; Ciesielski et al. 2019; Zhou et al. 2020). Usov et al. determined that the kinks are not a result of prior heterogeneity in the fibrils, rather a kink could be induced by processing at any location. Adding to these findings, Ciesielski et al. found that disorder could occur at the kink location, as a result of the mechanical deformation that formed the kink. These disordered sites were thought to be preferential sites for enzymatic hydrolysis, as indicated by selective thinning of fibrils near kinks, after enzyme exposure. Likewise, local disordered regions could become loci for failure in structural nanocomposites, while also limiting achievement of theoretical performance. As cellulose nanomaterials find application in functional devices ranging from gas barriers to piezo-actuators, thorough characterization of nanoscale defects in the material is essential to high-performance.

The inherent characteristics of cellulose (i.e., thin dimensionality, high stiffness and anisotropy) render mechanical property characterization challenging. Despite such challenges, previous studies have utilized atomic force microscopy (AFM) techniques to perform mechanical property measurements. For example, the elastic moduli of CNFs have been quantified using a nanoscale three-point bend technique (Guhados et al. 2005; Cheng and Wang 2008; Cheng et al. 2009; Iwamoto et al. 2009). Briefly, CNFs are dispersed on a substrate with pores or grooves, and a single CNF suspended between two points of contact is identified for measurement. Force spectroscopy is then used to obtain force and displacement data at points along the length of the suspended CNF. To determine the elastic modulus, the collected force and displacement data are analyzed using flexural beam theory. From previous studies, the elastic moduli are reported as (98 ± 6) GPa for Lyocell CNFs (i.e., regenerated cellulose), (81 ± 12) GPa for wood pulp CNFs, (84 ± 23) GPa for commercial microfibrilated CNFs (Cheng et al. 2009) and (78 ± 17) GPa for bacterial CNFs (Guhados et al. 2005). Notably, the three-point bend technique only measures properties averaged across the span length of a single fibril. Thus, it is not possible to identify local heterogeneities due to variation in crystallinity, damage or other defects.

Fewer AFM measurements have assessed the elastic modulus of cellulose supported on a solid substrate. Such measurements allow for the full resolution of AFM to be employed by revealing nanometer-scale heterogeneities. Using AFM force-distance curves and a finite element model, the transverse elastic modulus of wood CNCs at 0.1% relative humidity (RH) was reported to range from 18 to 50 GPa (Lahiji et al. 2010). Applying a similar approach, the transverse elastic modulus of tunicate CNCs at 0.1% RH was reported as 6 ± 6 GPa from AFM force-distance curves collected along the length of the CNC but analyzed using the Hertz-based DMT model (Postek et al. 2011). Wagner et al. (2016) used contact resonance force microscopy (CRFM) and contact mechanics models to measure and quantify the

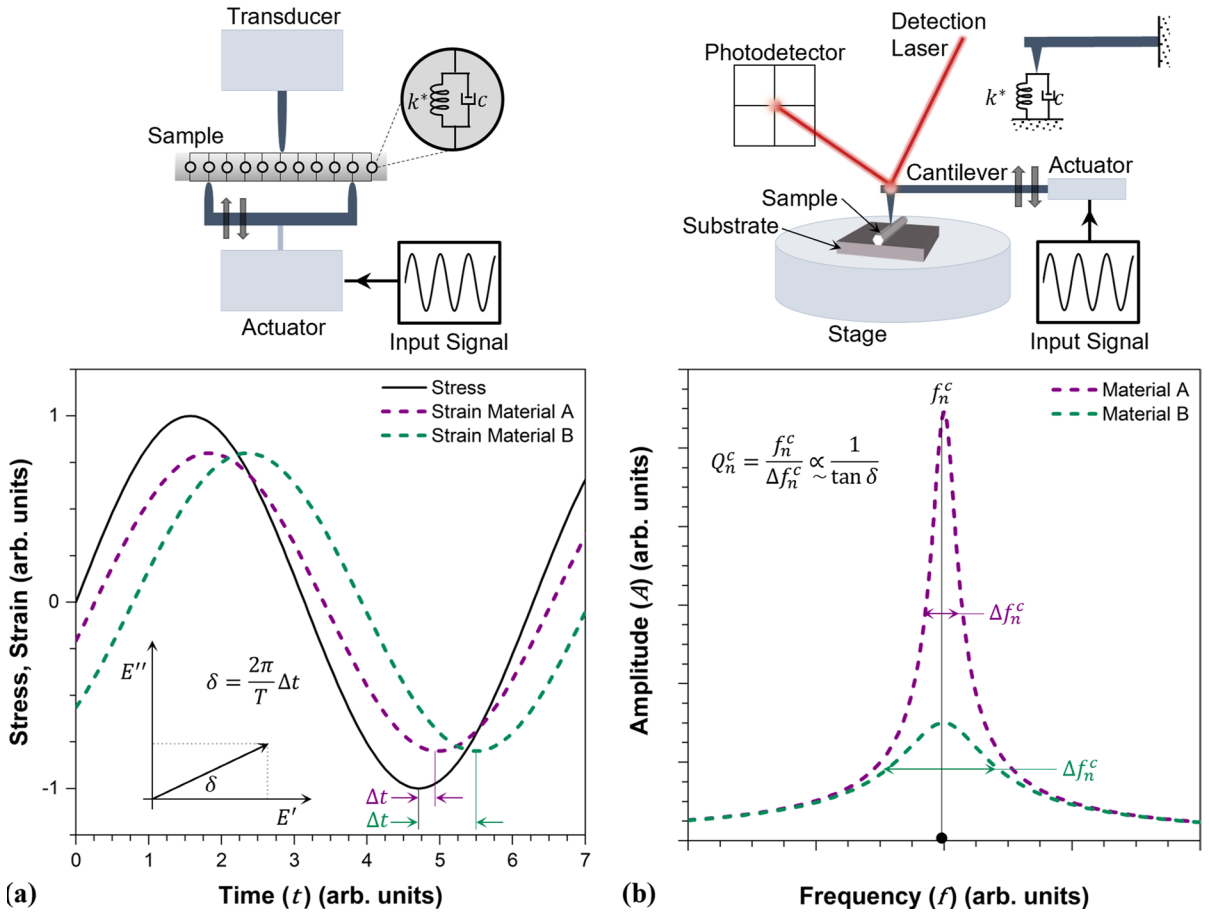

Fig. 1 Experimental set-up schematic and representative collected data for viscoelastic measurements of a sample using **a** DMA and **b** AFM where illustrative Material A has a higher tanδ compared to illustrative Material B

elastic modulus of wood CNFs. CRFM measures the resonance frequency of the AFM cantilever when the tip is in repulsive contact with the sample of interest. Variations in stiffness of the sample result in corresponding shifts in the resonance frequency, which can be translated into mechanical properties via models of the cantilever dynamics and contact mechanics. Compared to AFM force-distance, Wagner et al. (2016) demonstrated that CRFM afforded sufficient sensitivity due to the resonance enhancement to resolve the stiffness contrast between CNFs and substrate. However, the results were shown to vary by up to an order of magnitude depending on whether and how the applied contact mechanics model considered the thinness of the CNFs (Wagner et al. 2016).

Beyond the elastic CRFM measurements reported in (Wagner et al. 2016), CRFM also allows for the measurement of viscoelastic properties, such as storage modulus (E'), loss modulus (E''), and loss tangent (tanδ). This work seeks to address some of the limitations of prior CRFM work by operating with much lower total forces while simultaneously expanding the materials characterization to include viscoelasticity. Understanding the viscoelastic behavior of a material is important for material development and performance. Notably, the unexpected effects of viscoelastic behavior discovered during the usage of a material can be anticipated and mitigated. As shown in Fig. 1a, dynamic mechanical analysis (DMA) is a common technique to measure viscoelastic properties. To summarize, a sinusoidal stress is applied to a sample and the recorded strain response will lag by a phase angle (δ) that is related to the time lag (Δt). From the stress, strain and δ, the viscoelastic

properties of the sample can be calculated. E' is a measure of the stored energy and represents the elastic portion of the viscoelastic measurement. E'' is a measure of the dissipated energy and represents the viscous portion of the measurements. Finally, tanδ is a function of the elastic and viscous response, where $\tan\delta = E'/E''$, and provides a ratio of the dissipated and stored energy in the material (Lakes 2009). Although it is possible to perform sine-wave modulated viscoelastic measurements via AFM, the resultant phase lag measurements are often high noise and subject to considerable cross-talk (Hurley and Killgore 2013). CRFM can address these limitations by calculating tanδ from the quality factor (Q_n) and frequency (f_n) of the resonance peak at mode n (Hurley and Killgore 2013; Killgore and DelRio 2018). For comparison, traditional sine-wave modulated viscoelastic measurements (e.g., DMA and lower frequency AFM) are shown in Fig. 1a and CRFM viscoelastic measurements are shown in Fig. 1b where illustrative Material A and Material B have relatively low and high tanδ, respectively. It is seen that the modest shift in phase lag in Fig. 1a corresponds with a dramatic reduction in Q_n in Fig. 1b.

Applying viscoelastic CRFM methods to fragile, dimensionally constrained CNFs requires novel modifications of previous methods. The low-total-force (LTF) CRFM method developed here operates with the lowest total combined static and dynamic forces. LTF-CRFM measurements are performed at a static force close to the tip-sample adhesion force (i.e., low static force) and the cantilever is driven by Brownian motion (i.e., lowest dynamic force). Most often in AFM, Brownian motion or thermal noise excitation is used for well-established calibration methods to determine cantilever spring constant or optical sensitivity prior to AFM measurements (Hutter and Bechhoefer 1993; Sader et al. 1995; Proksch et al. 2004). However, some studies have found other advantages of using Brownian motion. Tung et al. (2014) used Brownian motion excitation to alleviate the "forest of peaks" and mitigate the fluid-born excitation phenomena for CRFM measurements of borosilicate glass samples immersed in water (Tung et al. 2014). In addition, Gonzalez-Martinez et al. (2019) used Brownian motion excitation to reduce damage when performing CRFM measurements on polyurethane (PU) samples. The technique was found to be sensitive to changes in the viscoelasticity in the PU films as relative humidity increased, as indicated by resonance peak shape and quantified tanδ values (Gonzalez-Martinez et al. 2019).

The above studies demonstrate some benefits of Brownian motion CRFM, which are expanded upon here with LTF-CRFM. First, LTF-CRFM improves linearity of the tip-sample contact, which is necessary to satisfy small amplitude approximations when calculating a sample stiffness and damping, especially at low static forces. Typically, with an external dynamic force (e.g., piezo actuation or photothermal) the tip-sample contact would be highly non-linear close to pull off because the dynamic force is of similar or greater magnitude to the static force. Second, LTF-CRFM minimizes the size of the stress field in the sample such that it is wholly contained within the CNF, similar to recent applications of low-force force-modulation AFM for of ultra-thin (< 10 nm) and ultra-hard (100–1000 GPa) 2D materials (Cellini et al. 2019). This mitigates modeling uncertainties when the sample is not an infinite half space and reduces systematic contributions of substrate properties to measured sample properties. Third, the low applied forces induce less sample damage from either static or dynamic indentation. Overall, when applied to CNFs, LTF-CRFM is shown to maintain tip-sample linearity, eliminate CNF damage, provide quantification of tan δ, and reveal that heterogeneity in CNFs is minimal, even in the vicinity of kinked defects.

Material and methods[1]

Materials

The materials for this study included cellulose nanofibrils, silicon wafers (Ted Pella, Redding, CA), and glass slides (Millipore Sigma, St. Louis, MO). The cellulose was purified by repeated boiling in 0.2 mol/m^3 NaOH for 6 h. The sample was then rinsed and immersed overnight in 0.1 mol/m^3 HCl at room

[1] Commercial equipment, instruments, or materials are identified only in order to adequately specify certain procedures. In no case does such identification imply recommendation or endorsement by the National Institute of Standards and Technology, nor does it imply that the products identified are necessarily the best available for the purpose.

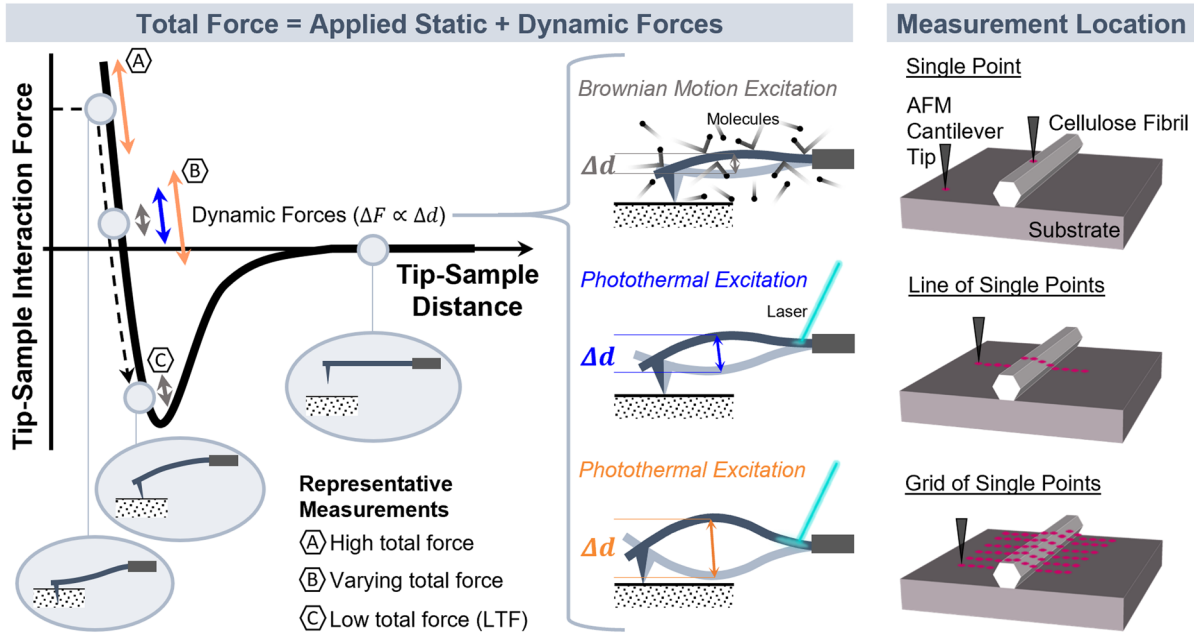

Fig. 2 Minimizing the applied static and dynamic forces to investigate LTF-CRFM measurements. The applied static force corresponds to points along the well-established tip-sample interaction curve where the static force is either incremented from or held at a starting static force. The applied dynamic force was minimized using Brownian motion excitation and compared to conventional photothermal excitation, where the dynamic force (ΔF) is proportional to the cantilever response amplitude (Δd) due to excitation. CRFM measurements were completed at a single point, over a line of single points, and over a grid of single points

temperature followed by thorough washing to neutral pH (Sugiyama et al. 1991). The resulting material was further purified by a treatment at 80 °C for 2 h in 0.25 wt% $NaClO_2$, washed and autoclaved in 1% H_2SO_4 at 121 °C for 1 h followed by thorough washing to neutral pH. The resultant purified cellulose sample was freeze dried and stored at room temperature for further use.

The fibril dimensions were characterized by AFM height measurement and transmission electron microscopy width measurement. The composition and morphology of the fibrils were analyzed by X-ray diffraction, nuclear magnetic resonance and acid hydrolysis.

LTF-CRFM nanomechanical measurements

CRFM experimental techniques and analysis are well documented within the literature (Rabe et al. 2000; Rabe 2006; Hurley and Killgore 2013). To summarize, the AFM cantilever is excited over a range of frequencies and the response spectrum is recorded. When the cantilever tip is vibrated in free space, resonant modes occur at certain frequencies depending on the cantilever shape and material. When the cantilever is vibrated with the tip in contact with the sample surface, the resonance occurs at a frequency that is greater than the free resonance frequency due to the stiffness of the tip-sample interaction. Using the free and contact resonance frequencies and appropriate beam-dynamics and contact-mechanics models material properties of the sample can be determined. In this work, the resonance peaks from resonant modes 1 and 3 were used for analysis.

Figure 2 illustrates LTF-CRFM nanomechanical measurements, where total force combines applied static and dynamic forces. To perform LTF-CRFM, the cantilever is excited using the lowest possible dynamic force (i.e., Brownian motion) at the lowest static force while still maintaining contact with the sample. Using Brownian motion to modulate the cantilever minimizes the oscillation range, while reducing the AFM deflection setpoint minimizes the static force. As such, LTF-CRFM simultaneously

minimizes the static and dynamic forces to perform nanomechanical measurements at the lowest total force and, consequently, the smallest induced stress field. For comparison to LTF-CRFM, traditional CRFM measurements were completed at higher static and dynamic forces, as shown in Fig. 2. Higher dynamic forces were achieved by photothermal excitation. The LTF-CRFM measurements were completed at single points, along a line of points, and across a grid of points.

Controlling the applied static force

The applied static force is determined by the product of the cantilever displacement and spring constant and controlled by the deflection setpoint. For many of the LTF-CRFM measurements, the static force is decremented from a starting value until the cantilever tip detaches from the surface. Detachment occurs when the combined static and dynamic forces exceed the adhesive force. Because the CNFs are relatively stiff and applied static forces are small and thus adhesive effects cannot be neglected, the CNF contact mechanics are approximated by the Derjaguin-Muller-Toporov (DMT) model. In the DMT model, tip-sample force is considered as a sum of applied force and adhesion force, which we refer to as the net force. In LTF-CRFM measurements performed at a single force, the adhesion force is not known, thus we only refer to the applied force. Whenever the tip was translated to a new measurement location it was fully withdrawn from the sample to minimize damage from lateral-forces.

Controlling the applied dynamic force using brownian motion and photothermal excitation

The applied dynamic force (ΔF) is a function of the cantilever's dynamic stiffness and the amplitude of any external drive force. Brownian motion excitation occurs independent of external drive force due to the thermal energy from the Brownian motion of molecules interacting with the cantilever and causing it to vibrate. This produces a white noise excitation over all possible frequencies, which translates into cantilever motion primarily at frequencies in the vicinity of the cantilever resonances. Thus, Brownian motion is the lowest possible dynamic force at a given temperature. To apply photothermal excitation, a power-modulated 405 nm laser is focused at the base of the cantilever and the absorbed energy causes the cantilever to vibrate at the modulation frequency. The modulation amplitude of the photothermal laser is used to control the dynamic force. In addition, the oscillation of the cantilever causes a corresponding cyclic fluctuation in the total force, as schematically depicted in Fig. 2. For example, decreasing ΔF proportionally decreases Δd, which reduces the fluctuation in total force at any static force along the tip-sample interaction curve.

Development and validation of LTF-CRFM nanomechanical measurements

Sample preparation and experimental set-up

Cellulose fibrils were dispersed using an aqueous solution on a UV-ozone- and plasma- treated silicon wafer or a UV-ozone- and plasma- treated glass slide. The AFM measurements were conducted at room temperature (≈18 °C) using a Cypher S AFM microscope (Asylum Research, Santa Barbara, CA). The AFM cantilevers (FM-AUD, Nanosensors, Switzerland) used in these methods had measured spring constants and first free resonances of ≈1.51 N/m and ≈53.3 kHz, ≈3.51 N/m and ≈76.3 kHz, and 3.61 ± 0.34 N/m and ≈80.3 kHz for the methods described in "Comparing LTF and traditional CRFM", "Evaluating CNF damage from LTF compared to increasing total force CRFM", "Using LTF-CRFM to quantify tanδ of CNFs on silicon and glass substrates" and "Using LTF-CRFM to map heterogeneity in tanδ along the length of a CNF" sections, respectively.

Using AFM tapping mode measurements to identify and observe isolated CNFs

Tapping mode measurements generated high-resolution images that were used to identify isolated CNFs for further investigation. First, 5 μm × 5 μm regions were scanned at 2.44 Hz with 19.5 nm pixel size until an area with well-dispersed CNFs was observed. Next, a 500 nm × 500 nm region of the identified isolated CNF was scanned. As needed, the region area, rate, and pixel size were tailored to generate an image that better resolved an isolated CNF for investigation. For all tapping mode measurements, the

typical setpoint amplitude was 60% of the free amplitude (≈ 50–100 nm) to ensure tip-sample interaction remained in the repulsive regime.

Comparing LTF and traditional CRFM

To compare the key CRFM measurands (i.e. frequency and quality factor) between LTF-CRFM and traditional CRFM, measurements were taken at four single points (Fig. 2) along the length of a CNF on a silicon substrate. For each single point CRFM measurement, three dynamic forces were applied over an incrementally decreasing range of static forces to investigate total forces. Brownian motion provided the lowest dynamic force ΔF_{BM} while low ΔF_{PT1} and high ΔF_{PT2} AC magnitudes of photothermal excitation provided comparative traditional CRFM results. The typical applied static force at the start of the force decrement was 8 nN or 17 nN, depending on the run, The Brownian motion spectra were recorded first by capturing a 5 MHz data stream for 1.72 s from the AFM's deflection photodetector, then performing a power spectrum analysis with a square window and 70 Hz frequency resolution. Next, the photothermal excited spectra were acquired with 1 s acquisition time, 2 ms lock-in time constant, and 100–200 kHz sweep-width for each drive amplitude. The applied static force was then decremented by 0.3–0.8 nN and the varied dynamic forces were applied again. This process was repeated until the tip detached from the sample.

Evaluating CNF damage from LTF compared to increasing total force CRFM

One potential benefit of LTF-CRFM is that the instantaneous maximum stress (i.e. the peak AC force superimposed on the static force) is reduced, correspondingly reducing the likelihood that the yield stress in the CNF is exceeded. Exceeding of the yield stress could result in permanent damage to the fibril. Thus, fibril damage was assessed after exposing the fibril to varying static and dynamic force. CRFM measurements were taken at single points) along the length of the identified CNF on silicon. Studies were performed with four starting applied static forces of 11.3 nN, 16.9 nN, 45.1 nN, and 84.6 nN, with Brownian motion (ΔF_{BM}) or photothermal (ΔF_{PT3}) dynamic excitation. ΔF_{PT3} had the same drive amplitude as ΔF_{PT2}, with slightly different resultant dynamic force due to the placement of the excitation laser on the cantilever. Before each CRFM measurement, tapping mode AFM images were acquired to identify a pristine section of the CNF. For the CRFM measurement, the cantilever tip started in contact at the desired applied static force and the response spectrum from ΔF_{BM} was recorded. The ΔF_{BM} acquisition was repeated at incrementally lower force setpoint until the tip detached. Next, tapping mode measurements were performed to obtain topographical data of the tested section of the CNF. If no damage was observed, the single point CRFM measurement was repeated at the same location and starting static force but applying ΔF_{PT3}. If damage was observed, the measurement location was moved to a pristine portion of the CNF. Single point CRFM measurements continued until each dynamic force and starting static force combination were completed.

Using LTF-CRFM to quantify tanδ of CNFs on silicon and glass substrates

To quantify tan δ on cellulose with LTF-CRFM, it was necessary to ensure that the AFM tip was accurately on the top of the cellulose fibril. If the tip is offset to either side of the fibril, the tip can slide and dissipate energy and correspondingly indicate higher tan δ. To ensure measurements were confidently located directly atop the fibril, a series of 25 Brownian motion LTF-CRFM measurements were performed perpendicular to the long axis of the fibril, extending from substrate to cellulose and back to substrate. The LTF-CRFM measurements include a height measurement to confirm location on the cellulose. The measurements were performed across five different CNFs. Two of the CNFs were on a silicon substrate, while the remaining three CNFs were on a glass substrate. The starting applied force was ≈20 nN and the force decrement was 2 nN.

Using LTF-CRFM to map heterogeneity in tanδ along the length of a CNF

Whereas the method in 2.3.5 provides high confidence for measuring the loss tangent atop the fibril at the lowest forces, it becomes excessively time consuming when applied to a 2D array of locations rather than a single cross section. To shorten the

measurement duration, 2D mapping was performed at only a single, ≈10 nN applied static force rather than with a force decrement. Tapping mode imaging was used to survey a large number of CNFs and identify those with good isolation and apparent kink formation. Four CNFs were mapped in this analysis via three image regions. Three maps were acquired with 50×50, 50×50, and 25×50 single points over 400 nm×400 nm, 175 nm×175 nm, and 100 nm×200 nm areas, respectively.

Data processing techniques

Four data processing techniques were selected and applied to the appropriate data sets. First, net and applied static force calculations were performed for all data sets. Second, the relative magnitude of the dynamic force was determined for the data sets involving multiple dynamic forces, as described in "Comparing LTF and traditional CRFM" and "Evaluating CNF damage from LTF compared to increasing total force CRFM" sections. Third, peak fitting functions were used for all data sets. Finally, the viscoelastic properties (i.e., tanδ and k^*)were determined for the data sets in "Using LTF-CRFM to quantify tanδ of CNFs on silicon and glass substrates" and "Using LTF-CRFM to map heterogeneity in tanδ along the length of a CNF" sections. A detailed explanation of the four data processing techniques including any relevant equations, tables, or figures is provided in Section S8.0 of the Supplementary Information (SI).

Results

Characterization of cellulose nanofibrils

From microscopy, the fibrils exhibit a hexagonal cross section, with 2 major axes. AFM height data indicate a mean height of 12 nm which is attributed to the shorter axis of the fibril. TEM data indicate a mean width of 22 nm which is attributed to the long axis. The crystallinity index of the cellulose was determined from X-ray Diffraction to be 91% and acid hydrolysis per NREL/TP-510-42618 revealed a Glucan content of 88%. Nuclear magnetic resonance spectrum of Cladophora cellulose showed Iα rich type cellulose such as those of bacterial and Valonia celluloses as reported previously (Atalla and Vanderhart 1984).

Response spectra analysis for LTF compared to higher total force CRFM

To evaluate the effect of total force on CRFM response, Fig. 3 shows the results from Brownian motion excitation (i.e., lowest dynamic force) compared to small and large amplitude photothermal excitations (i.e., increasing dynamic forces) as net force decreases from ~ 14 nN down to the tip-sample detachment force. Thus, analysis of Fig. 3 examines the lowest total forces at which quantifiable measurements can be obtained. The measurements reveal conditions of good and poor agreement between different excitation schemes, while also providing some guidance on mechanisms for the discrepancy in agreement. Quantification of dynamic force in CRFM is more challenging than for tapping-mode AFM because the contact-dependent-vibrational-shape affects the calibration of optical lever sensitivity in a difficult-to-predict fashion. Nonetheless, the relative amplitudes of cantilever motion can be compared at identical CR frequency to inform differences in dynamic force. The average relative magnitudes of the three dynamic forces increase from 1 to 53 to 550 for ΔF_{BM}, ΔF_{PT1} and ΔF_{PT2}, respectively (i.e. ΔF_{PT1} is ≈50× larger than the thermal limit and ΔF_{PT2} is 550× larger). Figure 3a shows mode 1 contact response spectra at a representative low (i.e., 1.2 nN) and high (i.e., 14 nN) static force and the three increasing dynamic forces (i.e., ΔF_{BM}, ΔF_{PT1}, ΔF_{PT2}). Figure 3a shows the contact resonance peaks fitted to the damped harmonic oscillator (DHO) model. The contact frequency (f_1^c) and quality factor (Q_1^c) results, shown in Fig. 3b, c, are obtained from the DHO model fit of each contact resonance peak.

Figure 3a shows the response spectra for Brownian motion (as power spectral density (PSD)) and photothermal excitation (as amplitude vs frequency) at 1.2 nN and 14.1 nN net static forces, with corresponding DHO model fits. At the higher static force of 14.1 nN, the contact resonance peaks for all dynamic forces are easily detectable. However, the contact resonance peak for the highest dynamic force (ΔF_{PT2}) shows a nonlinear response as evidenced by the asymmetric skew in the peak and the deviation from the DHO fit. At the lower static force of 1.2 nN, the peaks become

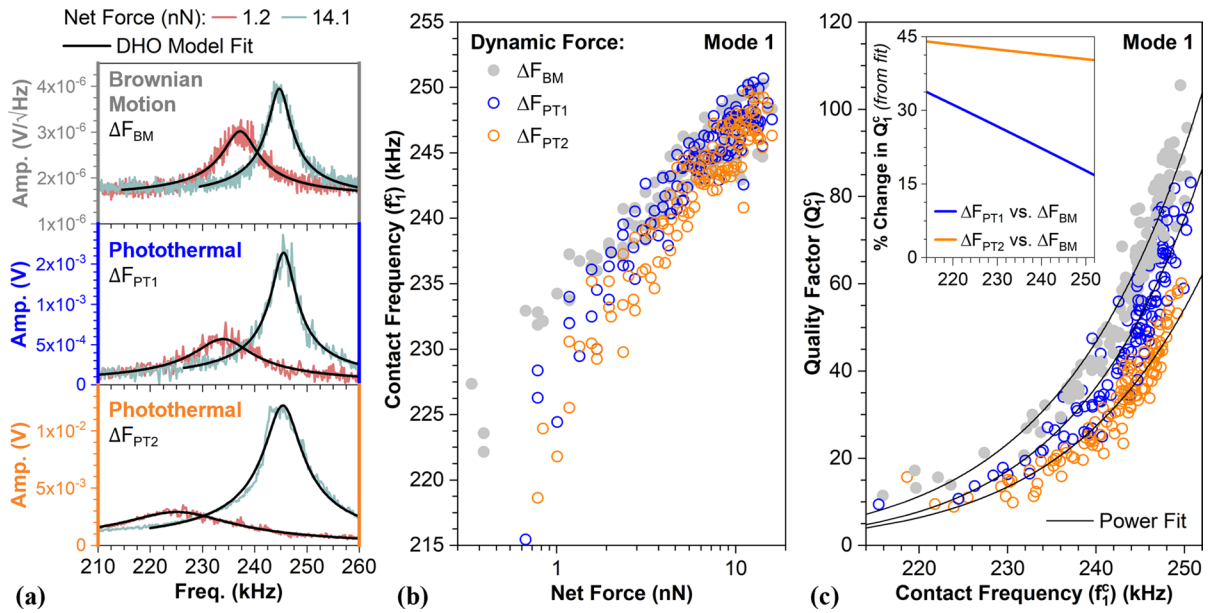

Fig. 3 Representative mode 1 contact response spectra fitted to the damped harmonic oscillator (DHO) model (**a**) from single point CRFM measurements at combinations of three increasing dynamic forces (where the lowest dynamic force uses Brownian motion and the two higher dynamic forces use photothermal excitation) and two net static forces (i.e., 1.2 and 14.1 nN). Mode 1 static force compared to contact frequency (**b**) and mode 1 contact frequency compared to quality factor (c) from single point CRFM measurements at four locations along the CNF length where the inset in **c** shows the percent error in the power fit between the photothermal (i.e., ΔF_{PT1} and ΔF_{PT2}) and Brownian motion (i.e., ΔF_{BM}) dynamic forces

broader (i.e. lower $Q_1{}^c$) as the dynamic force. In the absence of non-linear effects or varying contact properties (e.g., a changing AFM tip radius or varying sample viscoelasticity), it is expected that all three excitation techniques would result in identical f_1^c and Q_1^c results as a function of applied force. In the cases shown, the f_1^c and Q_1^c are reduced for the low static forces with larger amplitude photothermal excitation compared to the smaller excitation amplitudes. Although this non-linear effect at low static forces is less pronounced than the skew at higher force, it would directly affect calculated elastic and dissipative material properties. For example, an artifically lower f_1^c will falsely indicate a lower contact stiffness and thus Young's modulus of the surface (because net force and tip radius remain constant). An artificially lower Q_1^c, at the same resonance frequency, will falsely indicate a higher tanδ for the material. At the same time, the lower total forces will result in a more localized stress field within the cellulose. Thus, accuracy in interpreting the cantilever's dynamic response at low applied static force is essential to localized mechanical property measurements on geometrically confined materials. Given the apparent improvements in linearity of the resonance response with smaller excitation amplitude, we assert that more reliable characterization is possible with Brownian motion compared to larger amplitude excitation.

Figure 3b expands on this effect of total force on CR response by analyzing the mode 1 contact resonance spectra using the DHO fit while static force decreases at three dynamic forces. At high static force, all three dynamic forces produce similar and consistent f_1^c results, but high static forces induce a larger stress field from tip indentation compared low static forces. When the stress field is larger than the sample cross section, substrate effects need to be considered when evaluating the elastic modulus or loss tangent of the sample. Decreasing the static force mitigates substrate effects by limiting the stress field induced by the tip indentation to the sample cross section. However, the amplitude of the dynamic force can prevent the tip from maintaining linear contact with the sample at low static force. Compared to ΔF_{BM}, the higher dynamic forces (i.e., ΔF_{PT1} and ΔF_{PT2}) underestimate f_1^c as the static force

approaches zero, consistent with less linearity in the tip-sample contact.

Figure 3c shows Q_1^c as it relates to f_1^c for mode 1. At a given f_1^c, tanδ is inversely proportional to Q_1^c (Fig. 1b). Over the range of f_1^c, the Q_1^c trends higher as the applied dynamic force increases from ΔF_{BM} to ΔF_{PT1} to ΔF_{PT2}. To further analyze the difference in Q_1^c between the dynamic forces, a power fit was applied to each dynamic force data set. Then, as shown in the inset, the % change in Q_1^c was computed using the power fit to compare ΔF_{BM} to ΔF_{PT1} and ΔF_{PT2}, respectively. When compared to ΔF_{BM}, the % change in Q_1^c for ΔF_{PT1} and ΔF_{PT2} varies from 33 to 15% and 44% to 40%, respectively, as f_1^c increases from 215 to 255 kHz. A given % variation in Q_1^c between dynamic forcing schemes will result in a corresponding % variation in the calculated tanδ. For example, the use of ΔF_{PT2} would result in up to 44% higher apparent tanδ compared to ΔF_{BM}. Moreover, the % change in Q_1^c is higher for both ΔF_{PT1} and ΔF_{PT2} at lower static forces, which are preferable to reduce the indentation induced stress field.

Damage evaluation of CNFs from CRFM due to increasing applied total forces

In addition to localizing the stress field, total forces must also be considered in regard to potential damage they may inflict on the cellulose fibril. Varying the maximum applied dynamic and static forces used during single point CRFM measurements, followed by tapping mode topographic imaging, was used to observe any associated damage to the CNF. Figure 4a shows topographical tapping mode AFM images of the CNF before and after single point CRFM measurements were performed. The single point CRFM measurements were taken at the approximate locations denoted by triangles representing the cantilever tip. From the comparisons of topography before and after the measurement, it is clear that significant damage has occurred in the higher total force cases. The labeled sections A though E correspond to the approximate locations of the height profiles of the CNF in Fig. 4b. The starting static force for measurement locations within sections A, B, C, D, and E increased from 11.3 nN to 16.9 nN to 45.1 nN to 84.6 nN to 84.6 nN, respectively. For each section, the results show the height profile of the CNF before any CRFM measurements, after a single point CRFM measurement using ΔF_{BM}, and after a single point CRFM measurement using ΔF_{PT3}. For this comparison, the average relative magnitude of ΔF_{PT3} was calculated as $\approx$ 625 ΔF_{BM}, comparable to ΔF_{PT2} discussed in "Characterization of cellulose nanofibrils" section.

From Fig. 4a, the change in topography of the CNF from pristine to post-measurement condition shows evidence of damage due to total forces (i.e., combined static and dynamic), particularly on segments C and E. Height profiles along the length of the CNF (Fig. 4b) make the damage more apparent and allow assessment of whether the damage has occurred as a result of the static force or total force. The root mean square (RMS) roughness (Maradudin 2007) was computed for each height profile and reported in Fig. 4a. The average and standard deviation of the RMS roughness for all pristine sections ($\mu_{pristine} \pm \sigma_{pristine}$) is (0.26 ± 0.07) nm. If the post-measurement RMS roughness is greater than $\mu_{pristine} + 2 \cdot \sigma_{pristine}$ (i.e., 0.4 nm), damage is considered to have occurred. After ΔF_{BM} measurements, all sections at static forces ranging from 11.3 to 84.6 nN remain undamaged. After ΔF_{PT3} measurements, Sections A and B at static forces of 11.3 nN and 16.9 nN, respectively, remain undamaged, but Sections C and E at static forces of 45.1 nN and 84.6 nN, respectively, incur damage. At the lower static forces of 11.3 nN and 16.9 nN, ΔF_{PT3} measurements do not cause damage to the CNF, but resonance non-linearity is likely to occur and affect the accuracy of the result, as described in "Characterization of cellulose nanofibrils" section. At the higher static forces of 45.1 nN and 84.6 nN, ΔF_{BM} measurements do not cause damage to the CNF, but ΔF_{PT3} measurements do cause damage. It is notable that the static forces alone do not cause any damage in the static force range (i.e., 11.3 nN to 84.6 nN) investigated. Therefore, using Brownian motion as the dynamic force offers a non-damaging method of obtaining analyzable CRFM measurements of CNFs. It is notable that the occurrence of damage to the fibrils is a complex phenomenon that depends on magnitude of the applied forces, sharpness of the tip, and likely some characteristics of the specific CNF. Thus, the findings here are treated as representative of only a particular experimental condition which highlights the influence of the dynamic force.

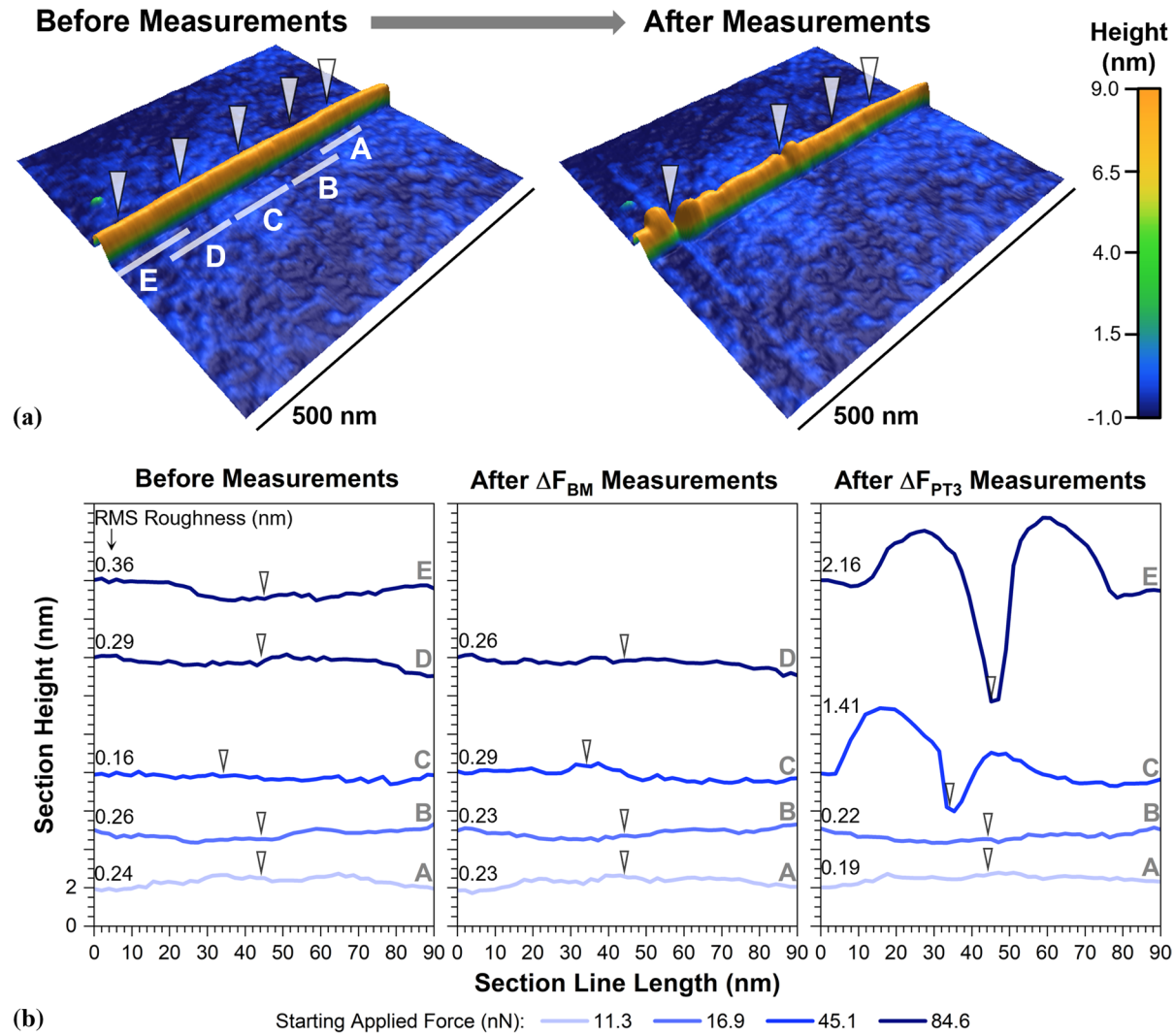

Fig. 4 Damage evaluation of a CNF from point measurements with varying static and dynamic forces. A topographical image of the CNF **a** is shown before and after measurements where the denoted sections correspond to the approximate lengths of the height profiles (**b**) that follow the top of the CNF. For each section with a corresponding starting static force, a height profile is shown before any measurements (left), after a point measurement using ΔF_{BM} (center), and after a point measurement using ΔF_{PT3} (right). Note, at 84.6 nN static force, two separate locations, D and E, were used for ΔF_{BM} and ΔF_{PT3}, respectively. The height profiles have been manually y-offset for clarity. The root mean square (RMS) roughness is shown to indicate change in the height profile

Quantifying *tanδ* of CNFs using LTF-CRFM

With some initial benefits of LTF-CRFM on CNFs established, the method was used to perform quantitative contact stiffness (k^*) and tanδ measurements on the cross section of the CNF. By traversing the cross section, the top surface of the CNF can be identified from the height profile and the ability to differentiate sample from substrate via LTF-CRFM can be ensured. Figure 5 shows the results from LTF-CRFM measurements that were taken at spot locations in a line over a CNF. Figure 5a, b show the height of the CNF on the z-axis, the net static force on the y-axis, and the lateral position on the x-axis for a representative single CNF. Correspondingly, the color scale in the images represents k^* and tanδ in Fig. 5a, b, respectively. The CNF is identified by its height above the substrate. For a given static force, the CNF has lower

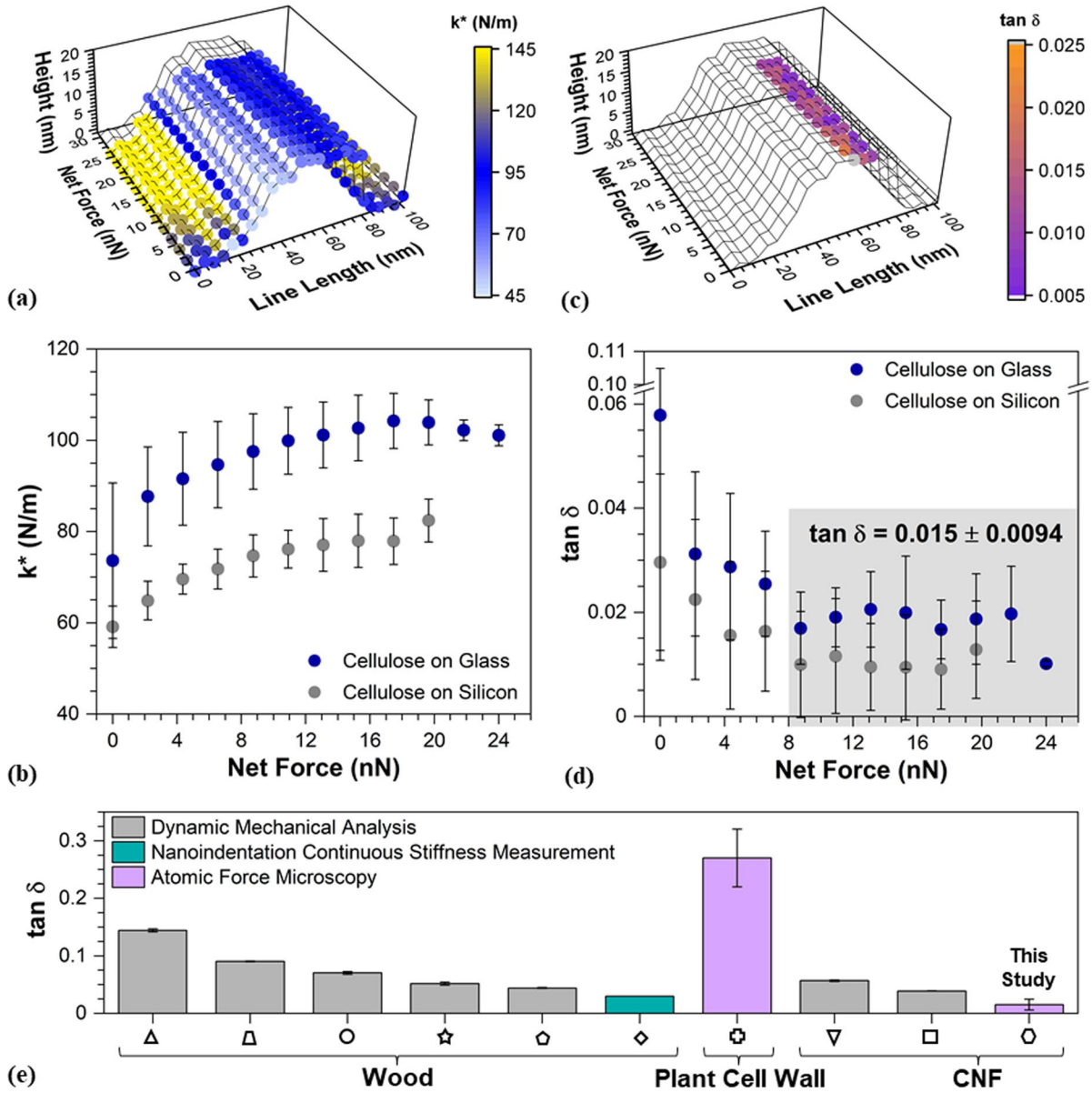

Fig. 5 Representative data for contact stiffness k^* (**a**) and loss tangent (**c**) from a single CNF on a glass substrate. The axes of the plot indicate lateral location of the measurement (line length), height at that location, and net static force. The color scale denotes the measurand of interest. Height data can be used to confirm that the measurands coincide with location on the top of the CNF. The compiled results (**b**, **d**) from the top of 3 separate CNFs on glass and 2 CNFs on silicon substrate as static force increases. The gray shaded region in **d** indicates the plateau values, all of which are averaged together to obtain the mean value tan $\delta = 0.015 \pm 0.0094$. **e** Shows the mean from all 6 plateau tan δ measurements from this study as it relates to previously published measurements using different experimental methods for woods: ulmus americana (△), pinus strobus (⏢), oak (○), beech (☆), spruce (⬠), carapa procera (◇); plant cell walls: arabidopis thaliana in water (✪); and CNFs: CNF and epoxy composite (▽), CNF sheet (□), and CNF (⬡) (Olsson and Salmén 1997; Placet et al. 2007; Zhang et al. 2012; Qing et al. 2015; Churnside et al. 2015; Venkatesh et al. 2018)

k^* than the substrate, and the k^* decreases as expected with decreasing static force. Some low-stiffness edge artifacts are observed when the tip interacts with the sides of the CNF, accordingly these measurements can be discarded based on the corresponding topography. The contrast in k^* between the CNF and substrate confirms mechanical sensitivity to the dimensionally confined CNFs, allowing viscoelastic tan δ analysis to proceed.

In Fig. 5b, the CNF tops are highlighted to reflect variations in tan δ with static force. tan δ measurements are generally independent of contact area, and thus expected to exhibit consistent value regardless of static force, assuming substrate-independence. As shown in Fig. 5c (where 5 total fibrils on either glass and silicon substrate were measured), tan δ measurements exhibit a force-dependence below ≈8 nN, then plateau to a value of 0.015 ± 0.0094. The higher tan δ trend observed below 8 nN is attributed to a contribution from surface water, which provides additional damping in the contact. This additional contribution is minimized at the higher forces, when material damping becomes the dominant signal. One consideration in the characterization of relatively low tan δ materials is whether the observed values are distinguishable from the low-damping noise floor of the measurement. For reference, additional k^* and tanδ results from glass and silicon substrate measurements have been provided in Figure S6. The CNF tanδ results (Fig. 5b) are greater than the substrate tanδ results using a blunted tip cantilever (Figure S6), which demonstrates that the cellulose tanδ does not reflect the lower-bound sensitivity threshold of the measurement.

In Fig. 5d, the measured tanδ from this study is compared to other reported tanδ values for different wood species, a plant cell wall, and fabricated CNF materials. The reported tanδ results were most commonly determined using dynamic mechanical analysis, but nanoscale tanδ results were also obtained using nanoindentation and AFM CRFM methods. Compared to wood species, the measured tanδ from this study is lower. This result is expected due to the cellular structure of wood and the presence of other lignocellulosic polymers, which would increase the damping in the material. As reported in (Churnside et al. 2015), CRFM has been previously used to measure the viscoelastic properties of other lignocellulosic materials. In this case, the tanδ of the plant cell wall from *Arabidopsis Thaliana* is much higher because the measurements were performed in water. When compared to fabricated CNF materials, the quantified tanδ from this study is lower which is likely due to the influence of the epoxy constituent and cellulose-cellulose interaction. The low value of tanδ from this study substantiates the crystalline molecular structure that occurs in CNFs (Moon et al. 2011).

Mapping *tanδ* of CNFs using LTF-CRFM

In addition to its utility for viscoelastic measurements at single locations or along section profiles, LTF-CRFM can also be applied in a mapping modality. Although it is possible to perform LTF-CRFM in arrays with the same varying static force regimen as above, such data sets take prohibitively long to acquire, and can experience unacceptable thermal drift as a result. For example, a single LTF-CRFM spectrum takes 1–3 s to acquire. Additional steps such as changing the force or withdrawing the tip and moving to a new location also add a few seconds, thus most of these measurements averaged ≈5 s per data point. Overall, this timing results in mapping durations on the order of a few hours depending on x–y resolution. The addition of ≈10 force decrements at each location shifts the measurement duration towards days. Thus, only a single ≈10 nN applied static force was employed during mapping. The applied static force was a compromise between feedback reliability and stress field optimization. Overall, the mapping tanδ values in Fig. 6 are slightly higher than measured in the full LTF-CRFM analysis in "Damage evaluation of CNFs from CRFM due to increasing applied total forces" section. However, considering the contact stiffness results in Fig. 5a showing contrast between CNF and substrate at similar static force, LTF-CRFM performed at a select static force can still reflect relative variations in CNF properties.

As an application of LTF-CRFM mapping, measurements sought spatial variations in tanδ associated with kinked defects, or 'kinks', along the CNF. Kinks in CNFs and CNCs have implications on biofuel production and nanomechanical composite reinforcement (Elazzouzi-Hafraoui et al. 2008; Usov et al. 2015; Chen et al. 2018; Ciesielski et al. 2019; Zhou et al. 2020). Previous work using molecular simulations showed that the

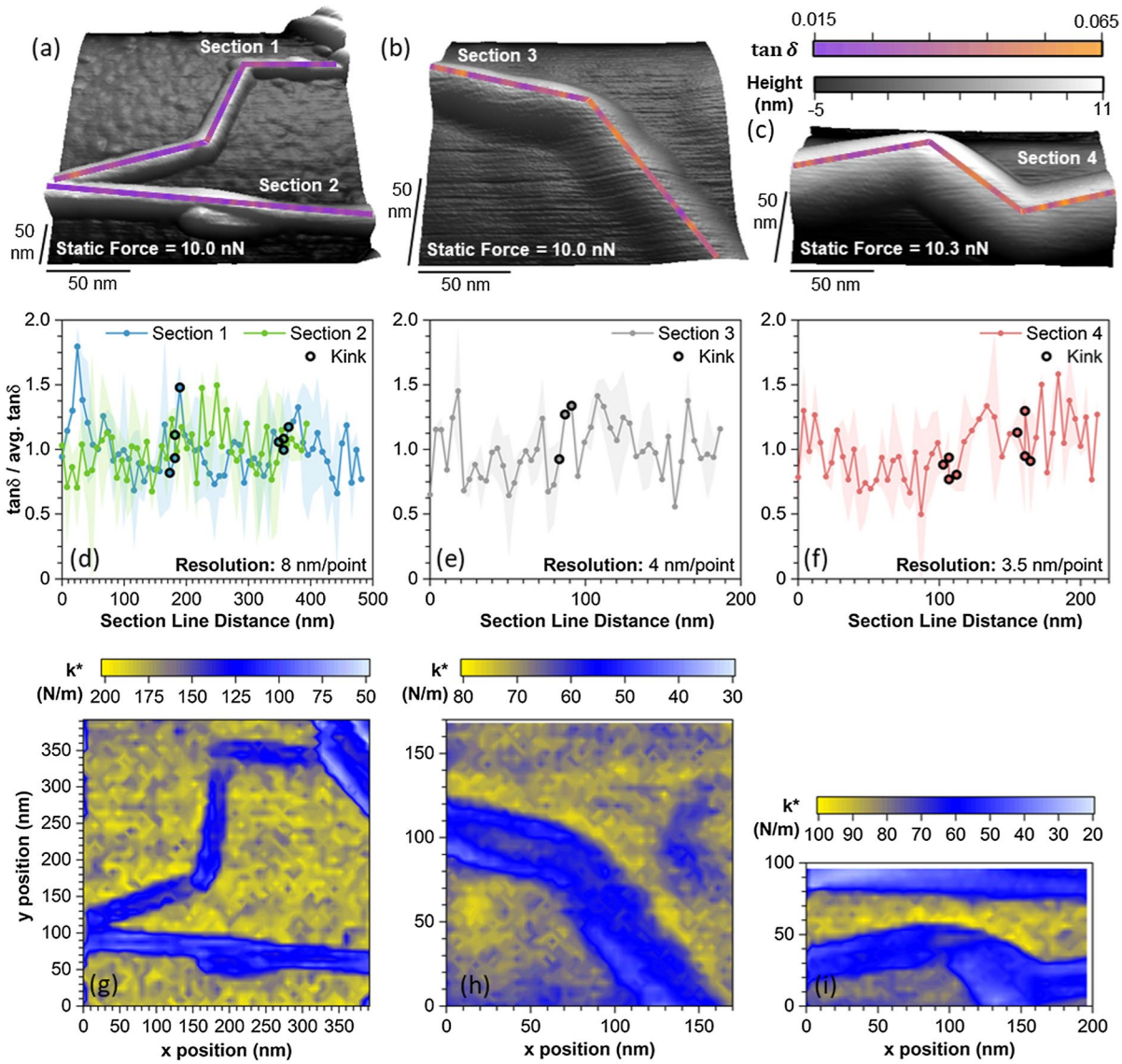

Fig. 6 AFM topographical images with LTF-CRFM tan δ color maps (**a**–**c**) of 4 selected CNF arrangements and corresponding line plots (**d**–**f**) of tanδ at points along the section line normalized by the average tanδ value for the entire section line. To determine tanδ along the top of the CNF, the computed tanδ was correlated to the height measurement taken within the same single point CRFM measurement. As such, the section lines along the CNFs shown in the AFM topographical images (**a**–**c**) correspond to the approximate location of the tanδ result and are shown for illustration. The average tanδ values are 0.028, 0.026, 0.041, and 0.041 for Sections 1, 2, 3, and 4, respectively. The plotted error represents the coefficient of variation. Circle markers in the bottom plots indicate data points proximal to the kink locations. The stiffness k^* maps acquired with LTF-CRFM are also shown (**g**–**i**), and clearly indicate the more compliant nature of the fibrils compared to the substrate

atomic structure of the CNF is highly ordered along the straight segments and relatively disordered at the kinks (Ciesielski et al. 2019). Of interest here was whether the disordered polymer chains at the kinks resulted in a detectable change in local tanδ values due to the presence of amorphous rather than crystalline structure. Transitions from amorphous to crystalline morphology are commonly characterized in semi-crystalline polymers undergoing cold-crystallization and can accompany an order of

magnitude increase in tan δ between the amorphous and crystalline states.

Four CNF arrangements, shown in Fig. 6, were identified for tanδ property mapping to analyze variation along the length of the CNFs. The selected CNFs have alignments with observable kinks or straight segments. In addition to selecting CNFs with different alignments, the resolution was also varied. For Sections 1 and 2, 2500 LTF-CRFM point measurements were taken over a 400 nm × 400 nm region resulting in a resolution of 8 nm/point. For Section 3, 2500 LTF-CRFM point measurements were taken over a 175 nm × 175 nm region resulting in a resolution of 4 nm/point. Finally, for Section 4, 1250 LTF-CRFM point measurements were taken over a 100 nm × 200 nm region resulting in a resolution of 3.5 nm/point. As such, the density of the LTF-CRFM point measurements was increased to further identify any material property variation along the CNFs.

Due to the aforementioned experimental drift, the height data collected during the LTF-CRFM measurements were used to identify the top of the CNF for tanδ property mapping. The tanδ results were averaged over two pixels wide for each position along the CNF length in order to obtain a mean and standard deviation. These mean tanδ values were then overlaid as color-scaled section lines on the corresponding higher-resolution tapping mode topography maps, as shown in Fig. 6a–c. As a representative example, the correlation between the LTF-CRFM height and tanδ results for Sections 1 and 2 is provided in Figure S7.

Figure 6d–f shows section profiles of the mapped tanδ results normalized by the average tanδ value for the entire section along the top of CNFs. The approximate kink locations are also indicated. The tanδ of the CNF in the vicinity of the kinks does not vary outside the bounds of the variability exhibited on the straight segments even as the pixel-resolution decreased from 8 nm/point to 3.5 nm/point. A statistical t-test analysis showed no significant difference ($p > 0.05$) in the mean tanδ between kink and straight locations along the four CNFs. The consistent tanδ results quantified herein provides increased confidence for applications requiring constant and reliable material properties, such the reinforcement constituent of composites materials, but suggests that higher resolution or enhanced sensitivity may be needed to resolve natural defects in the crystalline structure of cellulose. In (Ciesielski et al. 2019), for a CNF only 1–2 nm in width, the extent of the amorphized material was ≈ 3 nm for a 90° kink, which is less than the pixel spacing and contact-mechanics-imposed resolution in LTF-CRFM. Despite the prior possibility of a larger diameter CNF having a larger amorphized region at the kink, the tanδ results (Fig. 6) cannot prove such an effect. The disordered structure at the kink may be very localized and limited to the atomic scale or the nanoscale tanδ is dominated by lateral movement between the molecular chains and not influenced by the longitudinal order or disorder of the molecular chains. In (Ciesielski et al. 2019) it was also shown that kinks could be repaired by an AFM tip by dragging the kinked region back into alignment. However, it was not clear whether the apparent "repair" was superficial or extended to the molecular scale. For the process induced kinks in this present study, it may be that the crystalline structure has reformed at the kink, thus limiting their mechanical detection. Figure 6g–i shows contact stiffness k^* results on the fibrils. The fibrils are consistently less stiff than their substrates. Some low stiffness anomalies are observed near the kink locations, but they do not consistently align with the apex of the kink, thus more observations are likely needed to determine whether these low-stiffness regions are random, or coordinated with the kinks.

Conclusions

In this work, a new non-destructive LTF-CRFM was developed to quantify viscoelastic material properties, namely tanδ, of stiff rod-shaped CNFs with diameters ranging from 5 to 15 nm. LTF-CRFM uses Brownian motion to achieve the thermally limited lowest dynamic force, while approaching adhesive pull-off to achieve the lowest static force. First, LTF-CRFM measurements were shown to generate analyzable response spectra without evidence of nonlinear resonance softening. Second, CRFM measurements using Brownian motion did not damage CNFs for static forces ranging from 11.6 to 84.6 nN. Third, the quantified tanδ of CNFs is reported as 0.015 ± 0.0094 and demonstrates substrate independence within the standard deviation of the measurement. Finally, tanδ does not vary in the transverse direction over the length of CNFs with straight segments and kinks at the length scale of the measurement.

In conclusion, this work demonstrates the utility of LTF-CRFM for characterizing the viscoelastic material properties of thin and stiff nanoscale structures, such as CNFs. Moreover, LTF-CRFM can be applied to determine either localized tanδ at a single point location or more broadly to map variation in tanδ over an area of interest.

Acknowledgments This research was made possible by the National Institute of Standards and Technology, the Department of Civil, Environmental, and Architectural Engineering, the College of Engineering and Applied Sciences, and the Living Materials Laboratory (LMLab) at the University of Colorado Boulder with support from the National Science Foundation (Award No. CMMI-1537194).

Declarations

Conflict of interest There are no conflicts of interest to declare.

References

Atalla RH, Venderhart DL (1984) Native cellulose: a composite of two distinct crystalline forms. Science 223:283–285

Aydemir D, Gardner DJ (2020) The effects of cellulosic fillers on the mechanical, morphological, thermal, viscoelastic, and rheological properties of polyhydroxybutyrate biopolymers. Polym Composite 41:3842–3856. https://doi.org/10.1002/pc.25681

Azizi Samir MAS, Alloin F, Dufresne A (2005) Review of recent research into cellulosic whiskers, their properties and their application in nanocomposite field. Biomacromol 6:612–626. https://doi.org/10.1021/bm0493685

Cellini F, Gao Y, Riedo E (2019) Å-Indentation for non-destructive elastic moduli measurements of supported ultra-hard ultra-thin films and nanostructures. Sci Rep 9:4075. https://doi.org/10.1038/s41598-019-40636-0

Chen P, Ogawa Y, Nishiyama Y et al (2018) Iα to Iβ mechanoconversion and amorphization in native cellulose simulated by crystal bending. Cellulose 25:4345–4355. https://doi.org/10.1007/s10570-018-1860-x

Cheng Q, Wang S (2008) A method for testing the elastic modulus of single cellulose fibrils via atomic force microscopy. Compos Part A Appl S 39:1838–1843. https://doi.org/10.1016/j.compositesa.2008.09.007

Cheng Q, Wang S, Harper DP (2009) Effects of process and source on elastic modulus of single cellulose fibrils evaluated by atomic force microscopy. Compos Part A Appl S 40:583–588. https://doi.org/10.1016/j.compositesa.2009.02.011

Churnside AB, Tung RC, Killgore JP (2015) Quantitative contact resonance force microscopy for viscoelastic measurement of soft materials at the solid-liquid interface. Langmuir 31:11143–11149. https://doi.org/10.1021/acs.langmuir.5b02860

Ciesielski PN, Wagner R, Bharadwaj VS et al (2019) Nanomechanics of cellulose deformation reveal molecular defects that facilitate natural deconstruction. Proc Natl Acad Sci USA 116:9825–9830. https://doi.org/10.1073/pnas.1900161116

Curvello R, Raghuwanshi VS, Garnier G (2019) Engineering nanocellulose hydrogels for biomedical applications. Adv Colloid Interfac 267:47–61. https://doi.org/10.1016/j.cis.2019.03.002

Elazzouzi-Hafraoui S, Nishiyama Y, Putaux J-L et al (2008) The shape and size distribution of crystalline nanoparticles prepared by acid hydrolysis of native cellulose. Biomacromol 9:57–65. https://doi.org/10.1021/bm700769p

Gonzalez-Martinez JF, Kakar E, Erkselius S et al (2019) Effect of relative humidity on the viscoelasticity of thin organic films studied by contact thermal noise AFM. Langmuir 35:6015–6023. https://doi.org/10.1021/acs.langmuir.8b04222

Guhados G, Wan W, Hutter JL (2005) Measurement of the elastic modulus of single bacterial cellulose fibers using atomic force microscopy. Langmuir 21:6642–6646. https://doi.org/10.1021/la0504311

Heinze T (2015) Cellulose: structure and properties. In: Rojas OJ (ed) Cellulose chemistry and properties: fibers, nanocelluloses and advanced materials. Springer, Cham, pp 1–52

Hurley DC, Killgore JP (2013) Dynamic contact AFM methods for nanomechanical properties. In: Yablon DG (ed) Scanning probe microscopy in industrial applications. Wiley, Hoboken, pp 115–149

Hutter JL, Bechhoefer J (1993) Calibration of atomic-force microscope tips. Rev Sci Instrum 64:1868–1873. https://doi.org/10.1063/1.1143970

Iwamoto S, Kai W, Isogai A, Iwata T (2009) Elastic modulus of single cellulose microfibrils from tunicate measured by atomic force microscopy. Biomacromol 10:2571–2576. https://doi.org/10.1021/bm900520n

Killgore JP, DelRio FW (2018) Contact resonance force microscopy for viscoelastic property measurements: from fundamentals to state-of-the-art applications. Macromolecules 51:6977–6996. https://doi.org/10.1021/acs.macromol.8b01178

Lahiji RR, Xu X, Reifenberger R et al (2010) Atomic force microscopy characterization of cellulose nanocrystals. Langmuir 26:4480–4488. https://doi.org/10.1021/la903111j

Lakes R (2009) Dynamic behavior. In: Viscoelastic materials, Cambridge University Press

Maradudin AA (ed) (2007) Light scattering and nanoscale surface roughness. Springer, New York

Mariano M, Kissi NE, Dufresne A (2014) Cellulose nanocrystals and related nanocomposites: review of some properties and challenges. J Polym Sci Pol Phys 52:791–806. https://doi.org/10.1002/polb.23490

Moon R, Martini A, Nairn J et al (2011) Cellulose nanomaterials review: structure, properties and nanocomposites. Chem Soc Rev 40:3941–3994. https://doi.org/10.1039/C0CS00108B

Nechyporchuk O, Belgacem MN, Bras J (2016) Production of cellulose nanofibrils: a review of recent advances. Ind

Crop Prod 93:2–25. https://doi.org/10.1016/j.indcrop.2016.02.016
Nishiyama Y (2009) Structure and properties of the cellulose microfibril. J Wood Sci 55:241–249. https://doi.org/10.1007/s10086-009-1029-1
Olsson A-M, Salmén L (1997) The effect of lignin composition on the viscoelastic properties of wood. Nord Pulp Pap Res J 12:140–144. https://doi.org/10.3183/npprj-1997-12-03-p140-144
Placet V, Passard J, Perré P (2007) Viscoelastic properties of green wood across the grain measured by harmonic tests in the range 0–95°C: Hardwood vs. softwood and normal wood vs. reaction wood. Holzforschung 61:548–557. https://doi.org/10.1515/HF.2007.093
Postek MT, Vladár A, Dagata J et al (2011) Development of the metrology and imaging of cellulose nanocrystals. Meas Sci Technol 22:024005. https://doi.org/10.1088/0957-0233/22/2/024005
Proksch R, Schäffer TE, Cleveland JP et al (2004) Finite optical spot size and position corrections in thermal spring constant calibration. Nanotechnology 15:1344–1350. https://doi.org/10.1088/0957-4484/15/9/039
Purandare S, Gomez EF, Steckl AJ (2014) High brightness phosphorescent organic light emitting diodes on transparent and flexible cellulose films. Nanotechnology 25:094012. https://doi.org/10.1088/0957-4484/25/9/094012
Qing Y, Cai Z, Wu Y et al (2015) Facile preparation of optically transparent and hydrophobic cellulose nanofibril composite films. Ind Crop Prod 77:13–20. https://doi.org/10.1016/j.indcrop.2015.08.016
Rabe U, Amelio S, Kester E et al (2000) Quantitative determination of contact stiffness using atomic force acoustic microscopy. Ultrasonics 38:430–437. https://doi.org/10.1016/S0041-624X(99)00207-3
Rabe U (2006) Atomic force acoustic microscopy. In: Applied scanning probe methods II, Springer, pp 37–90
Sader JE, Larson I, Mulvaney P, White LR (1995) Method for the calibration of atomic force microscope cantilevers. Rev Sci Inst 66:3789–3798. https://doi.org/10.1063/1.1145439
Sugiyama J, Persson J, Chanzy H (1991) Combined infrared and electron diffraction study of the polymorphism of native celluloses. Macromolecules 24:2461–2466. https://doi.org/10.1021/ma00009a050
Tung RC, Killgore JP, Hurley DC (2014) Liquid contact resonance atomic force microscopy via experimental reconstruction of the hydrodynamic function. J Appl Phys 115:224904. https://doi.org/10.1063/1.4882755
Usov I, Nyström G, Adamcik J et al (2015) Understanding nanocellulose chirality and structure–properties relationship at the single fibril level. Nat Commun 6:7564. https://doi.org/10.1038/ncomms8564
Venkatesh A, Thunberg J, Moberg T et al (2018) Cellulose nanofibril-reinforced composites using aqueous dispersed ethylene-acrylic acid copolymer. Cellulose 25:4577–4589. https://doi.org/10.1007/s10570-018-1875-3
Wagner R, Moon RJ, Raman A (2016) Mechanical properties of cellulose nanomaterials studied by contact resonance atomic force microscopy. Cellulose 23:1031–1041. https://doi.org/10.1007/s10570-016-0883-4
Zhang T, Bai SL, Zhang YF, Thibaut B (2012) Viscoelastic properties of wood materials characterized by nanoindentation experiments. Wood Sci Technol 46:1003–1016. https://doi.org/10.1007/s00226-011-0458-3
Zhang Y, Nypelö T, Salas C et al (2013) Cellulose nanofibrils. J Renew Mater 1:195–211. https://doi.org/10.7569/JRM.2013.634115
Zhou Y, Ono Y, Takeuchi M, Isogai A (2020) Changes to the contour length, molecular chain length, and solid-state structures of nanocellulose resulting from sonication in water. Biomacromol 21:2346–2355. https://doi.org/10.1021/acs.biomac.0c00281